SPECIAL

Oceanic Flow—Topography Interactions

COLLECTION

Observation of Near-Inertial Waves in the Bottom Boundary Layer of an Abyssal Seamount

XIAOHUI XIE,[a,b,c] YAN WANG,[d] ZHIYU LIU,[e] XIAOHUI LIU,[a,c] DAKE CHEN,[a,b,c] DONGSHENG ZHANG,[a,b,c] AND JIANNAN WANG[a]

[a] *State Key Laboratory of Satellite Ocean Environment Dynamics, Second Institute of Oceanography, Ministry of Natural Resources, Hangzhou, China*
[b] *School of Oceanography, Shanghai Jiao Tong University, Shanghai, China*
[c] *Southern Marine Science and Engineering Guangdong Laboratory, Zhuhai, China*
[d] *Department of Ocean Science, Hong Kong University of Science and Technology, Hong Kong, China*
[e] *State Key Laboratory of Marine Environmental Science, and Department of Physical Oceanography, College of Ocean and Earth Sciences, Xiamen University, Xiamen, China*

ABSTRACT: The bottom boundary layer (BBL) contributes significantly to the global energy dissipation of low-frequency flows in the abyssal ocean, but how this dissipation occurs remains poorly understood. Using in situ data collected near the BBL at an abyssal seamount in the western Pacific Ocean, we demonstrate that strong bottom-trapped flows over sloping topography can lose their energy to near-inertial waves (NIWs) generated via the adjustment of the bottom Ekman layer. The NIWs with near-resonant frequencies corresponding to internal waves with propagation direction parallel to the topographic slope are observed. These waves are strongest in the BBL and have a correlation with the off-seamount subinertial flows largely attributed to the Ekman transport driven by the bottom-trapped anticyclonic circulation over the seamount. The bottom-intensified NIWs are observed to have dominant upward-propagating energy and hypothesized to be generated via Ekman flow–topography interactions in the BBL. Energy loss from the near-bottom flows to radiating NIWs ($\sim 8 \times 10^{-4}$ W m^{-2}) is estimated to be substantially larger than that due to bottom drag dissipation ($\sim 2 \times 10^{-4}$ W m^{-2}), suggesting the important role of internal-wave generation via the Ekman transport adjustment in damping the subinertial flows over the sloping seafloor.

SIGNIFICANCE STATEMENT: Dissipation of geostrophic currents and eddies via the oceanic bottom boundary layer (BBL) plays an important role in modulating the global oceanic mechanical energy budget. The bottom drag has long been considered a key process in inducing such dissipation, but it is recently suggested to be less effective at a sloping bottom. This study suggests another potentially important mechanism that can remove energy from the geostrophic flows at the sloping bottom. This mechanism is depicted as the resonant generation of near-inertial internal waves by near-bottom flows. Generation of internal waves due to near-bottom flows over sloping topography should be common in the global ocean and therefore have significant implications for the oceanic mechanical energy budget.

KEYWORDS: Bottom currents; Ekman pumping/transport; Internal waves; Topographic effects

---

1. Introduction

The bottom boundary layer (BBL) plays a vital role in damping oceanic geostrophic currents and eddies via bottom drag and thus in modulating the global oceanic mechanical energy budget (Wunsch and Ferrari 2004; Trowbridge and Lentz 2018). Wunsch and Ferrari (2004) suggested a global energy dissipation of ~0.2 TW in the abyssal BBL, while other estimates of this dissipation reach ~0.8 TW (Sen et al. 2008; Wright et al. 2013). This large uncertainty sources partly

from the presence of Ekman arrest over sloping topography (MacCready and Rhines 1991, 1993). When an along-isobath interior flow resides over a sloping bottom boundary, it can induce a cross-isobath bottom Ekman transport. The Ekman transport brings fluid either upward or downward at the sloping boundary and gives rise to a buoyancy forcing that opposes the Ekman transport, leading to the so-called Ekman arrest (MacCready and Rhines 1991; Garrett et al. 1993). During Ekman arrest, along-isobath flow is weakened toward the bottom, leading to the reduction of the bottom drag–induced dissipation. Using high-resolution numerical simulations, Ruan et al. (2021a) suggested much less bottom drag–induced energy dissipation of the geostrophic flows over

---

Corresponding author: Xiaohui Xie, xhxie2013@gmail.com

continental slopes in the Atlantic Ocean than that estimated from interior velocities.

Although direct bottom drag dissipation may not be as strong as previously suggested over sloping topography, other processes during the adjustment of the bottom Ekman layer also contribute to the turbulent dissipation in the BBL. In the downslope case, Ekman transport brings light water beneath dense water and thus triggers convective instabilities that drive turbulent mixing in the BBL (Garrett et al. 1993; Moum et al. 2004). Using high-resolution numerical simulations, several studies have reported that bottom-trapped currents flowing in the direction of Kelvin wave propagation along sloping topography are susceptible to submesoscale (symmetric and/ or centrifugal) instabilities, leading to enhanced turbulent mixing within the BBL (Dewar et al. 2015; Gula et al. 2016; Wenegrat and Thomas 2020). Recent field observations in the Southern Ocean provided evidence that the downslope Ekman transport may generate lateral density fronts near the bottom, fueling submesoscale instabilities and thus enhancing near-boundary turbulent mixing (Naveira Garabato et al. 2019). In addition to convective and submesoscale instabilities, numerical simulations also revealed that near-inertial waves (NIWs; i.e., internal waves with frequencies close to the local inertial frequency f) can be resonantly generated in the BBL during Ekman arrest over the sloping bottom (Brink and Lentz 2010; Umlauf et al. 2015; Ruan et al. 2019). However, there is as yet no observational evidence of NIW generation in the BBL via the cross-isobath Ekman transport.

Wind forcing has long been recognized to be the dominant mechanism generating downward-propagating NIWs near the sea surface [Alford et al. (2016) and the references therein], while bottom-generated NIWs are expected to radiate upward into the ocean interior (Nikurashin and Ferrari 2010a). The bottom generation and subsequent upward propagation of NIWs have also been observed, especially near rough topography (Brearley et al. 2013; Sheen et al. 2013; Liang and Thurnherr 2012; Hu et al. 2020). However, these observations have not pointed out potential NIW generation due to Ekman adjustment within the BBL. Instead, they seemed to have exclusively attributed NIWs generated near rough topography to internal lee-wave breaking (Nikurashin and Ferrari 2010a,b), despite the absence of a direct link between lee waves and NIWs in the observations. On the other hand, upward-propagating NIWs observed near rough topography may also source from the bottom reflection of wind-driven downward-propagating waves (Kunze and Sanford 1986) or geostrophic adjustment of the deep boundary flows (van Aken et al. 2005). In this study, we present observational evidence linking the generation of upward-propagating NIWs to the adjustment of the bottom Ekman layer over the sloping seafloor, highlighting the importance of internal-wave generation in the energy decay of near-bottom low-frequency flows.

2. Theoretical background

Over a flat seafloor, the bottom Ekman layer height H_E may be estimated using the scaling proposed by Weatherly and Martin (1978):

$$H_E = H_{WM} = 1.3(C_d U_\infty^2)^{1/2}(1 + N_\infty^2/f^2)^{-1/4}/f, \quad (1)$$

where U_∞ and N_∞ are the velocity and buoyancy frequency above the bottom Ekman layer, and C_d is the quadratic drag coefficient. In this study, C_d is set to be 0.0025 following previous studies of the abyssal ocean (Sen et al. 2008; Wright et al. 2013; Polzin et al. 2021). For a sloping seafloor (with a slope of α), no theoretical basis yet exists to estimate H_E because of its temporal variability during Ekman arrest. However, if the steady Ekman arrest state is reached, H_E can be approximated as the arrested Ekman layer thickness, which, in the downslope case, can be scaled by (Trowbridge and Lentz 1991; Ruan et al. 2019)

$$H_a = fU_\infty/\alpha^2 N_\infty^2. \quad (2)$$

Before the steady state is achieved, the Ekman transport at the sloping bottom can be estimated by (Brink and Lentz 2010)

$$T_E = fC_d U_\infty^2/(f^2 + \alpha^2 N_\infty^2). \quad (3)$$

Because the downslope Ekman transport thickens the BBL (MacCready and Rhines 1991; Garrett et al. 1993), H_{WM} and H_a will be treated as the lower and upper bounds for our estimation of H_E, respectively. To facilitate the comparison between theory and observation, we also use H_m to denote the height of the bottom mixed layer, with the squared buoyancy frequency $N^2 < 1 \times 10^{-7}$ s^{-2}. In the flat-bottom case, H_m is generally assumed to be equal to H_E, while H_m may be larger than H_E over the sloping bottom (Stahr and Sanford 1999).

The Ekman adjustment process over the sloping bottom may resonantly generate internal waves, as described by the following equations:

$$\frac{\partial^2 V}{\partial t^2} + \omega_c^2 V = f\frac{\partial \tau_x}{\partial z} - \frac{\partial^2 \tau_y}{\partial z \partial t} - \frac{\partial G}{\partial z}\alpha,$$
$$\omega_c^2 = f^2 + N_\infty^2 \alpha^2, \quad (4)$$

where V is defined as the cross-isobath low-frequency velocity; $[\tau_x, \tau_y]$ are the along-isobath and cross-isobath components of frictional stress; and G is the turbulent buoyancy flux [see Eq. (27) of Umlauf et al. 2015]. Equation (4) suggests that the bottom Ekman flow driven by an along-isobath interior flow over the slope can induce buoyancy fluxes, which in turn induce the temporal variations in Ekman flows and bottom stresses associated with the resonant-frequency ω_c. Therefore, internal waves with ω_c may be resonantly generated in the BBL, and their propagation direction is in parallel to the slope. When the slope is gentle (viz., small α), ω_c is close to f. Internal waves caused by the Ekman flow over the sloping bottom can be regarded as near-inertial waves. This process resembles the generation of near-inertial waves at the sea surface via time-varying winds. By contrast, over a flat bottom, the steady Ekman transport can be rapidly set up and no internal waves are generated (Garrett et al. 1993).
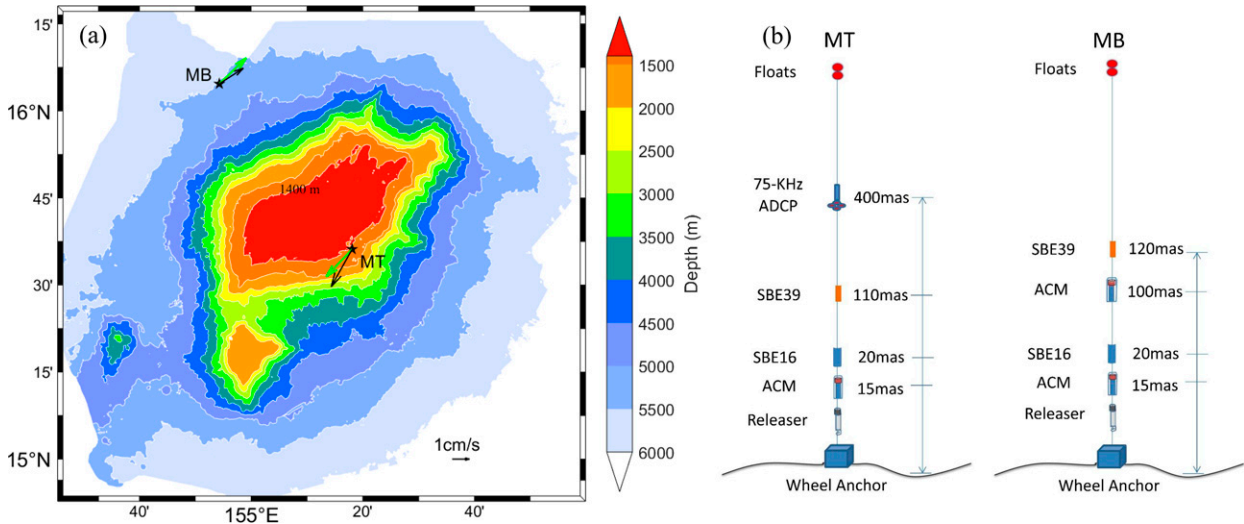
FIG. 1. (a) Map showing the bathymetry of the Caiwei Seamount in the western Pacific Ocean, two moorings (MT and MB; stars), and time-averaged near-bottom velocity vectors (arrows). The isobath of 1400 m is labeled. Black and green arrows are velocity vectors at the depths of 15 and 100 MAS, respectively. (b) Schematic of the moorings at MT and MB.

3. Data and methods

a. Data

Moored observations of the current and temperature/salinity were carried out at three sites over the Caiwei Seamount (CS) in the northwest Pacific Ocean (Fig. 1). One site was located at the top of the CS (denoted as site MT), where the topographic slope is ∼0.015, and the other two were at the base, with a topographic slope of ∼0.05. Because the two sites at the base were displaced by only ∼3 km and their water depths were almost identical (only ∼10 m difference), they were jointly denoted as site MB (Fig. 1a). Both MT and MB were equipped with an Aanderaa current meter (ACM) at 15 m above the seafloor (MAS) and a Sea-Bird SBE 16 with conductivity–temperature–depth (CTD) sensors at 20 MAS (Fig. 1b). At MB, an ACM fixed at 100 MAS and a Sea-Bird SBE 39 with temperature–depth (TD) sensors installed at 120 MAS were also deployed. At MT, a downward-looking 75-kHz acoustic Doppler current profiles (ADCP) and a Sea-Bird SBE 39 were installed at 400 and 110 MAS, respectively. The observation period of MB spanned from 15 June 2013 to 17 July 2014, while at MT it ranged between 23 July 2014 and 21 July 2015. However, data collected by the ACM at 15 MAS at MB became unavailable after 9 January 2014. Three ACMs recorded data every 30 min, whereas SBE 16 and SBE 39 sampled every 60 and 10 min, respectively. At MT, the ADCP recorded data every 30 min with 16-m vertical bins, covering the depth range of 1004–1356 m (∼40 MAS). Above the ADCP at this site, there were other moored instruments for current and temperature measurements, which are not used in this study. In addition, a Sea-Bird 917 CTD with a 24-Hz sampling rate was lowered to a depth of ∼30 MAS at MT and MB before the moorings were deployed. These two yo-yo CTD casts were used to estimate the buoyancy frequency N at the two mooring sites.

Horizontal velocities are decomposed into the along-isobath u and cross-isobath v components based on the bathymetry (Fig. 1). When positive v is defined to be outward perpendicular to the seamount isobaths, positive u is consistent with a clockwise flow around the seamount. The bathymetry used in this study is based on our shipboard sonar measurements (Fig. 1).

b. Decomposition of signals

In this study, we focus mainly on NIWs and low-frequency flows. These flow components in the raw current time series are extracted via a second-order Butterworth filter. Cutoff frequencies of near-inertial velocities $[u_f, v_f]$ are set to be $[0.85, 1.4]f$, and the low-frequency flow $[U, V]$ is extracted using the low-pass filter with a cutoff frequency corresponding to a period of 3 days.

4. Results

a. Background currents

Previous studies have suggested that a strong anticyclonic circulation can be generated near the bottom at the CS (Guo et al. 2020; Jiang et al. 2021; Xie et al. 2022), as observed at MT and MB where U (>0) often dominates over V (Figs. 2a,b and 3a,b). The anticyclonic flow may have induced an off-seamount Ekman transport ($V > 0$), which was observed at 15 MAS at both sites (Figs. 2b, 3b). At the summit of the seamount (MT), the annual-mean cross-isobath velocity was approximately 0.7 cm s^{-1} at 15 MAS, and cases with $V > 0$ occupied more than 70% of the yearlong observation period (Fig. 2b). Following Eqs. (1) and (2) and taking $U_\infty = 0.05$ m s^{-1} and $N_\infty^2 = 4 \times 10^{-6}$ s^{-2} at MT, H_{WM} and H_a are estimated to be 11 and 33 m, respectively. The range of the bottom Ekman layer height from the seafloor $[H_{WM}, H_a]$ covered 15 MAS but excludes the depth of bottommost ADCP measurement (40 MAS), at which point the cross-isobath flow vanished as
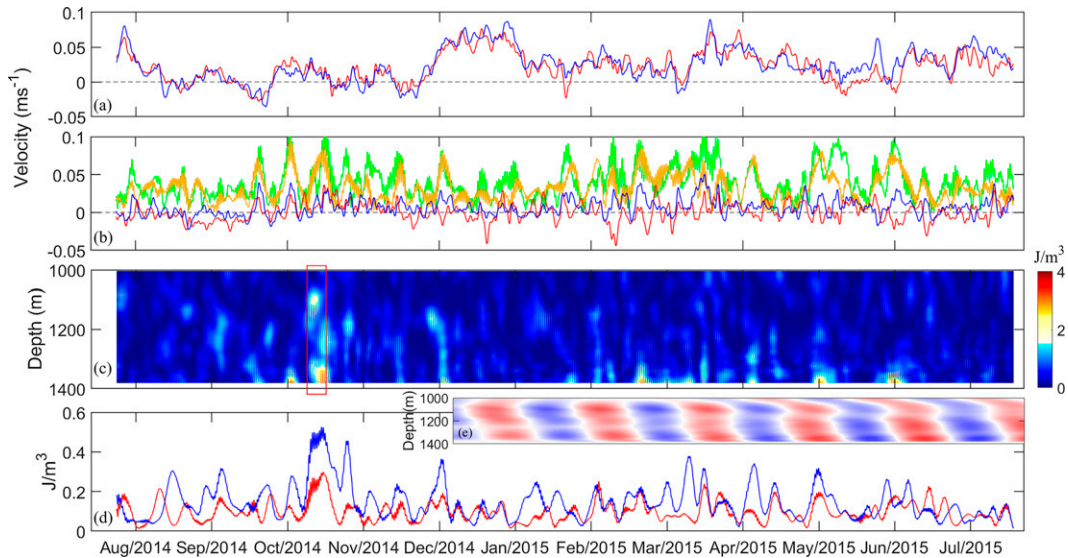
FIG. 2. (a) Time series of low-pass-filtered along-isobath velocity U at the depths of 15 (blue) and 40 MAS (red) at MT. (b) Low-pass-filtered cross-isobath velocities V at the depths of 15 (blue) and 40 MAS (red). The green and yellow lines are near-inertial velocity magnitude in the frequency bands of 0.85–1.4f (A_f) and 1.12–1.4f (A_{rf}) at 15 MAS, respectively. (c) Depth–time map of kinetic energy in the near-resonant frequency band of 1.12–1.4f (KE$_{rf}$). (d) Time series of depth-averaged upward- (blue) and downward-traveling (red) KE$_{rf}$. (e) Time–depth diagram of near-resonant inertial velocities u_{rf} in the period marked by the red rectangle in (c).

shown by the time-mean velocity field ($V < 0.1$ cm s^{-1}). Therefore, the flow at 40 MAS was almost parallel to the isobaths (Fig. 1a). The Ekman velocity T_E/H_E based on Eq. (3) is estimated to vary between 0.3 and 0.9 cm s^{-1}, consistent

with the observation. Following the enhanced off-seamount Ekman flows, an up-seamount compensating flow was often observed above the bottom Ekman layer (e.g., 40 MAS; Fig. 2b), indicating a secondary circulation in the cross-isobath
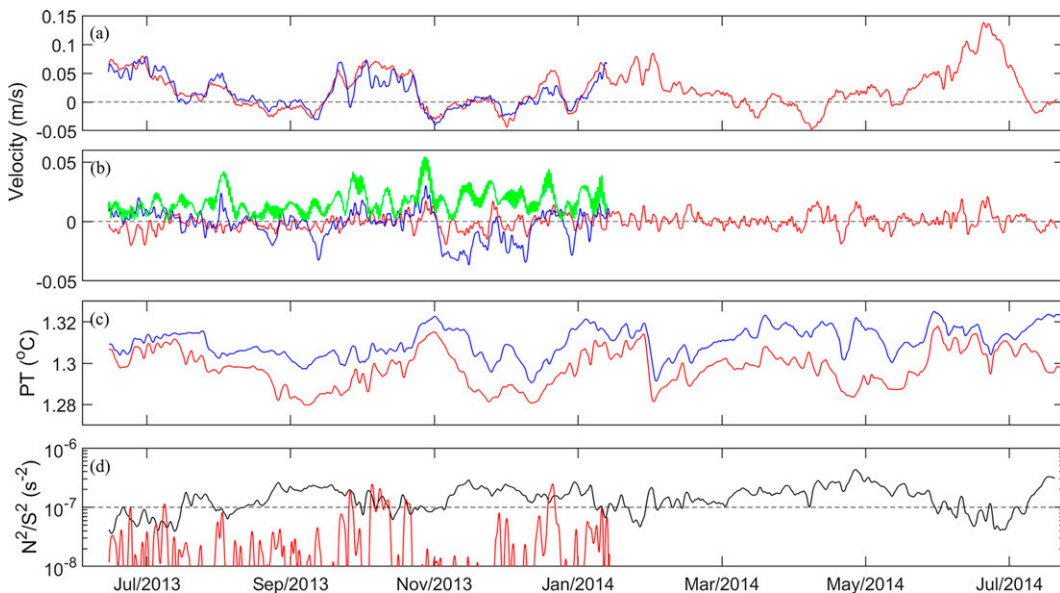

FIG. 3. (a) Time series of low-pass-filtered along-isobath velocities U at the depths of 15 (blue) and 100 MAS (red) at MB. (b) Low-pass-filtered cross-isobath velocities V at the depths of 15 (blue) and 100 MAS (red). The green line is near-inertial velocity magnitude A_f at 15 MAS. (c) Low-pass-filtered potential temperature at 20 (red) and 120 MAS (blue). (d) Time series of near-bottom stratification N^2 (black) computed from mooring CTD (20 MAS) and TD (120 MAS) data and squared geostrophic vertical shear [$S_g^2 = (\partial U/\partial z)^2$; red].
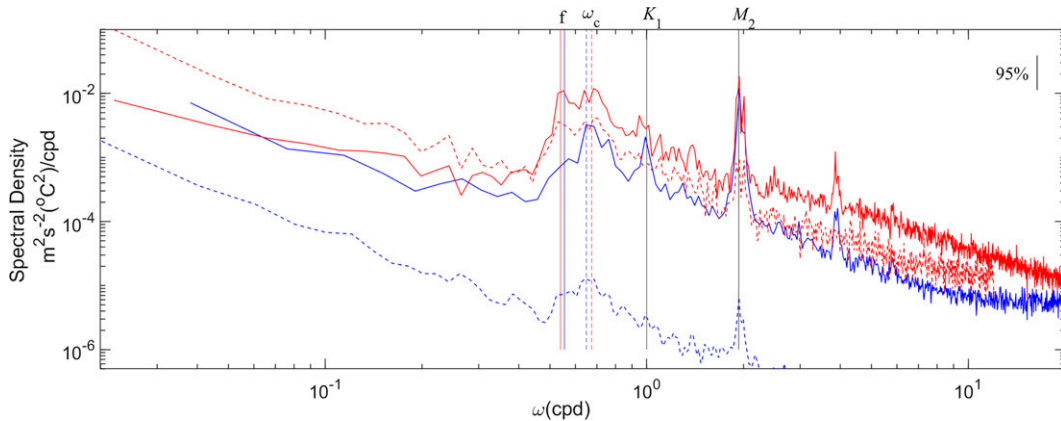
FIG. 4. Kinetic energy (solid) and temperature anomaly (dashed) spectra at the depth of 15 MAS at MT (red) and MB (blue). Vertical solid and dashed lines indicate the inertial frequency f and topographic resonant frequency ω_c, respectively, at MT (red) and MB (blue). Diurnal tidal component K_1 and semidiurnal tidal component M_2 are also labeled. The 95% statistical significance level is indicated by the vertical bars near the right-upper corner.

vertical plane, resembling those observed near the summit of other seamounts (Haidvogel et al. 1993; Freeland 1994; Lavelle and Mohn 2010). It should be noted that the off-seamount velocity was still visible at some times when the anticyclonic flow disappeared. Therefore, other processes may also contribute to the cross-isobath flow in the BBL.

At the base of the CS (MB), H_{WM} and H_a were estimated as 24 and 197 m, respectively. This depth range was large, covering two ACMs at this site. However, the time-mean velocity at 15 MAS concealed the bottom Ekman transport (i.e., the cross-isobath velocity was oriented up-seamount; see Fig. 1a), but events of $V > 0$ can be identified in the presence of anticyclonic jets (Figs. 3a,b), implying that bottom boundary processes may be dominated by the Ekman dynamics at some times while they became more complex at other times. At 100 MAS of this site, the cross-isobath velocities could frequently counter the off-seamount Ekman flows, suggesting that H_E may not exceed 100 m. Therefore, the theoretically estimated Ekman velocity at MB ranges between 0.1 and 0.5 cm s^{-1}. This estimate agrees with the observation at 15 MAS, where the cross-isobath velocity, averaged over the periods with $U > 2$ cm s^{-1}, was 0.3 cm s^{-1}. At 100 MAS, the time-mean cross-isobath velocity $V = -0.22$ cm s^{-1} (for $U > 2$ cm s^{-1}) opposed the off-seamount Ekman velocity, suggesting that the secondary circulation driven by the Ekman transport might not be confined to regions around the summit of seamount but occupy the entire seamount slope.

The off-seamount Ekman transport driven by anticyclonic flows brought light fluid downslope at the base of the seamount, leading to the increase of potential temperature observed at depths of both 20 and 120 MAS at MB (cf. Figs. 3a,c). Moreover, the potential temperature difference between the two depths was substantially lessened (<0.01°C) so that near-bottom stratification was nearly eroded in the presence of anticyclonic flows ($N^2 < 1 \times 10^{-7}$ s^{-2}; Fig. 3d). This suggests the enhancement of turbulent mixing and thickening of the bottom mixed layer ($H_m > 100$ m). Such a destratification process was also frequently observed across continental shelves when the

downshelf Ekman flows driven by along-shelf currents are predominant (Lentz and Trowbridge 1991), suggesting the occurrence of the bottom Ekman adjustment at MB (Garrett et al. 1993). At MT, the downslope transport of light water during $V_c > 0$ was scarcely observed from the CTD measurements at 20 MAS (not shown), which may be because the bottom Ekman layer was too thin ($H_E < 20$ m) to cover our instrument throughout most of the observational period.

b. Generation and propagation of near-inertial waves

As reviewed in section 2, the Ekman transport across the sloping bottom may generate NIWs with resonant frequency ω_c (Brink and Lentz 2010; Umlauf et al. 2015). Kinetic energy spectra computed from current records at the bottom boundary (15 MAS) are shown in Fig. 4 (solid curves). Dominant spectral peaks were identified at the semidiurnal tidal and near-inertial frequencies for both sites. At MT, there were two peaks in the f band: one was centered at f (1.00 ± 0.02f), and the other was blue shifted to ~1.25f. At MB, the peak frequency approached 1.19f. Near-inertial peaks were also observed in the temperature variance spectra (doted curves in Fig. 4), with peak frequencies almost identical to those observed in the kinetic energy spectra. The temperature variance spectra at both sites showed larger near-inertial energy than tidal energy, suggesting the presence of vigorous near-inertial waves. The blue-shifted peaks at MT (1.25f) and MB (1.19f) were approximately equal to ω_c, which was estimated to be 1.26f and 1.15f at MT and MB, respectively, following Eq. (4). Therefore, it can be reasonably hypothesized that NIWs with ω_c observed in the BBL mainly resulted from topographic resonance (Umlauf et al. 2015).

The enhanced near-inertial velocities near the bottom boundary were quantitatively related to the cross-isobath subinertial flows (Figs. 2b, 3b and 5a). At MB, the bottom-enhanced near-inertial velocities ($A_f = \sqrt{u_f^2 + v_f^2}$) were often phase locked with $V > 0$ in time, with the correlation coefficient of 0.20 for the 7-month-long record quantified using the
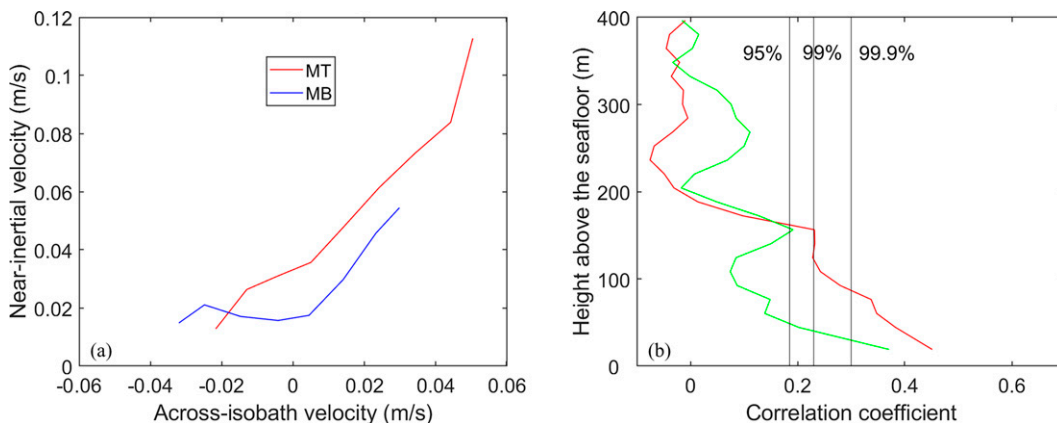
FIG. 5. (a) Averaged A_f against V (1 cm s^{-1} velocity bin) at MT (red) and MB (blue). (b) Depth profiles of correlation coefficients between A_{nrf} $[= \sqrt{(u_f - u_{rf})^2 + (v_f - v_{rf})^2}]$ (green)/A_{rf} (red) and V at 15 MAS at MT. The vertical lines indicate three statistical significance levels.

MATLAB function of "corrcoef (A_f, V)," where A_f and V are averaged every 2 days. This correlation was significant only at the 95% significance level. The correlation between V and A_f observed in the BBL was more robust at MT because of the almost one-to-one correspondence between two quantities ($\sim$70% of all enhanced events) in the yearlong observation period. Their correlation coefficient reached 0.62 and was significant at the 99.9% significance level. At both sites, A_f closely followed the velocity magnitude of the off-seamount flows (Fig. 5a). These observations provide support to our hypothesis that NIWs with the frequency of ω_c observed near the bottom boundary mainly resulted from the bottom Ekman adjustment.

Another spectral peak in the f band at MT was also observed at a frequency very close to f (Fig. 4). To rule out the effect of these signals centered at f and characterize vertical propagation of NIWs resulting from the bottom Ekman adjustment, the near-resonant velocities [u_{rf}, v_{rf}] in the frequency band of [1.12–1.4]f are separated from [u_f, v_f]. After removing the near-inertial signals centered at f, near-resonant inertial velocities ($A_{rf} = \sqrt{u_{rf}^2 + v_{rf}^2}$) were still correlated to the cross-isobath flows in the BBL (Fig. 2b), although the correlation coefficient decreased to $\sim$0.45 (Fig. 5b). The significant correlation coefficient between near-resonant inertial and cross-isobath low-frequency velocities in the BBL at the 99% significance level can be extended to 150 MAS, but it decreased away from the BBL. This was associated with upward propagation of NIWs resonantly generated in the BBL as documented next.

The near-resonant inertial kinetic energy [KE$_{rf}$ = $\rho(u_{rf}^2 + v_{rf}^2)/2$, where ρ = 1034 kg m^{-3} is seawater density] increased toward the BBL, where year-mean KE$_{rf}$ reached 0.65 J m^{-3} (Fig. 6a). Away from the bottom, kinetic energy was reduced by $\sim$50%, suggesting that wave energy may be significantly dissipated near the bottom. The bottom enhancement of near-resonant inertial signals can also be identified in the time–depth map of KE$_{rf}$ (Fig. 2c). Furthermore, these waves often showed dominant upward (downward) energy (phase) propagation (Fig. 2e).

Using a two-dimensional (ω_c and k_z) Fourier filter, the near-resonant inertial velocities [u_{rf}, v_{rf}] are decomposed into [u_{rf}^+, v_{rf}^+] with upward energy propagation $k_z^* + \omega_c t$ and [u_{rf}^-, v_{rf}^-] with downward energy propagation $k_z^* - \omega_c t$, where k_z is the vertical wavenumber (Pinkel 1984). The results also showed that upward-propagating energy was commonly higher than downgoing energy (Fig. 2d; upward-propagating energy was $\sim$50% stronger than its downgoing counterpart upon annal average), suggesting that near-resonant inertial waves are generated in the BBL and subsequently radiate upward into the ocean interior. Since the propagation slope β $[= \sqrt{(\omega^2 - f^2)/N^2 \omega_c}]$ (with respect to the horizontal direction) of internal waves generated
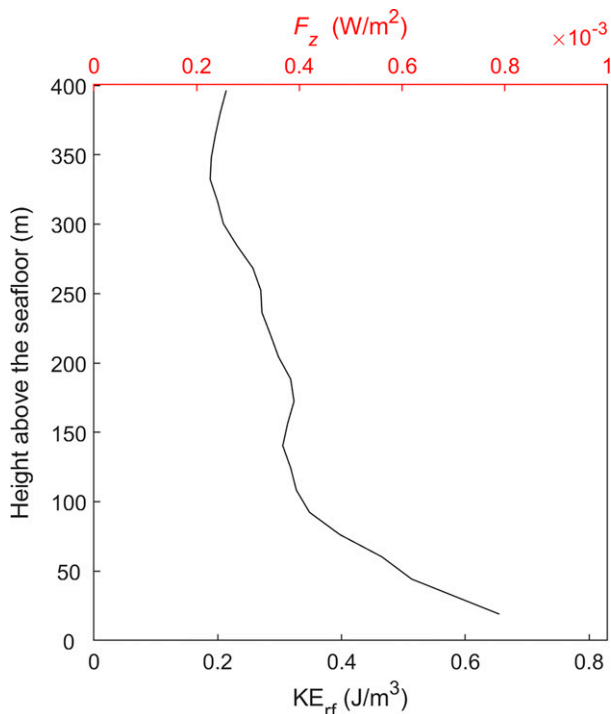

FIG. 6. Depth profiles of time averaged KE$_{rf}$ and F_z at MT.

by the topographic resonance is equal to the topographic slope [Eq. (4)], they may propagate upslope or downslope. However, internal waves with downslope propagation would soon encounter the weaker stratification at deeper levels, where β is larger than the topographic slope so that the waves may be reflected upward into the ocean interior. This may explain why the observed near-resonant inertial waves were predominantly upward propagating.

For the nonresonant inertial motions ($[u_f - u_{rf}, v_f - v_{rf}]$) at MT, namely, those with spectral peak centered at f, no significant correlation was detected between their velocities and the bottom Ekman transport, except at 15 MAS (Fig. 5b). These NIWs centered at f mainly resulted from nonlinear forcing of geostrophic flows over the large-scale seamount (Xie et al. 2023). We note that NIWs can be modulated by the background flows (e.g., negative vorticity induced by anticyclonic flows) so that their frequency band may be broadened (van Haren 2004). Therefore, the motions centered at f cannot be completely separated from the near-resonant inertial waves so that these motions still showed significant correlation with the off-seamount flows in the BBL (correlation coefficient = 0.37; Fig. 5b), where NIWs associated with other generation mechanisms were weak (not shown).

Another mechanism for the near-bottom generation of NIWs is the breaking of internal lee waves induced by geostrophic flows over sloping topography (Nikurashin and Ferrari 2010a). Although the cross-isobath Ekman flows may drive internal lee waves (Xie et al. 2017; Xie and Li 2019), the velocity amplitude of NIWs driven by wave breaking is comparable to that of the geostrophic flow (Nikurashin and Ferrari 2010b), which is therefore inconsistent with our observation that near-inertial velocities were often much stronger than the cross-isobath velocities (Figs. 2b, 3b). Furthermore, this mechanism cannot explain the resonant generation of NIWs in the BBL over the slope. Using profiled current observations, Kunze and Sanford (1986) showed that the reflection of wind-generated downward-propagating NIWs at critical topography may also induce dominant upward-propagating near-inertial energy around seamounts. However, the strong correlation between the bottom-enhanced near-inertial velocities and cross-isobath Ekman flows at MT ruled out the possibility of near-bottom reflection of wind-driven downward-traveling NIWs (Figs. 5a,b).

5. Discussion

a. The impact on dissipation of near-bottom geostrophic flows

Frictional drag has been suggested to be a key mechanism for damping the near-bottom geostrophic flows in the abyssal ocean (Wunsch and Ferrari 2004). As energy dissipation D caused by the bottom frictional drag can be approximated as $D = \rho C_d |U_\infty|^3$, the importance of resonant NIW generation as a process to remove energy from the bottom-trapped anticyclonic flows may be evaluated against that due to the work done by bottom friction. Energy transfer from the near-bottom

flows to resonant NIWs can be estimated via the vertical energy flux F_z of these waves, calculated as

$$F_z = C_{gz}\mathrm{KE}_{rf}, \quad C_{gz} = \frac{\omega_c^2 - f^2}{\omega_c^2}C_{pz}, \tag{5}$$

where C_{gz} and C_{pz} are the vertical group and phase speeds, respectively. We calculate D and F_z based on the data collected at MT, where C_{pz} can be estimated by the phase difference between near-resonant inertial velocities at different depths using the cross-correlation method. Upon averaging through the depths below 1300 m, we obtain $C_{gz} = 104$ m day^{-1}. The depth profile of year-mean F_z is plotted in Fig. 6. In the BBL (i.e., 15 MAS), the vertical wave flux reached 8.0×10^{-4} W m^{-2}, whereas the energy dissipation due to bottom drag was estimated to be 2.0×10^{-4} W m^{-2}. Therefore, NIWs radiating from the boundary flows were 4 times as large as the energy dissipation induced by the bottom drag at MT, suggesting that resonant generation of internal waves by the boundary flow–topography interaction likely plays an important role in damping the low-frequency flows at sloping bottom boundary.

b. Submesoscale instabilities

The observations at MB have shown that the BBL was significantly thickened ($H_m \gg H_{WM}$) in the presence of anticyclonic jets, suggesting that the near-bottom jets may have caused strong dissipation and mixing in the BBL. It is unclear whether this destratification process is associated with resonant NIWs, but previous field observations (Moum et al. 2004; Naveira Garabato et al. 2019; Xie et al. 2022) and numerical models (Wenegrat and Thomas 2020) suggested that downslope Ekman transports may induce convective and submesoscale instabilities that enhance bottom dissipation and mixing. The simulations in Wenegrat and Thomas (2020) also produced near-inertial oscillations with $\omega_c = 1.17f$ (see their Fig. 2a; J. Wenegrat 2022, personal communication), indicating the coexistence of NIWs and instabilities in the BBL during the bottom Ekman adjustment. Although the potential temperature difference between 20 and 120 MAS at MB in the presence of anticyclonic jets was substantially lessened, such a vertical displacement of measurement (100 m) prevents the identification of small-scale overturns (convective instability). Nevertheless, it is possible to make some speculations for the development of larger-scale submesoscale processes. In what follows, we discuss the possibilities of the occurrence of submesoscale instabilities based on the limited moored records.

To examine the possibilities of submesoscale instabilities, we calculated the Ertel potential vorticity (PV) based on along-isobath velocity U at MB where the bottom mixed layer and Ekman adjustment are both identifiable:

$$\mathrm{PV} = -f\left(\frac{\partial U}{\partial z}\right)^2 + \left(f - \frac{\partial U}{\partial y}\right)N^2. \tag{6}$$

For stably stratified flows (i.e., $N^2 > 0$) with PV < 0, submesoscale centrifugal and symmetric instabilities can occur (Thomas et al. 2013). For an anticyclonic circulation, its relative vorticity
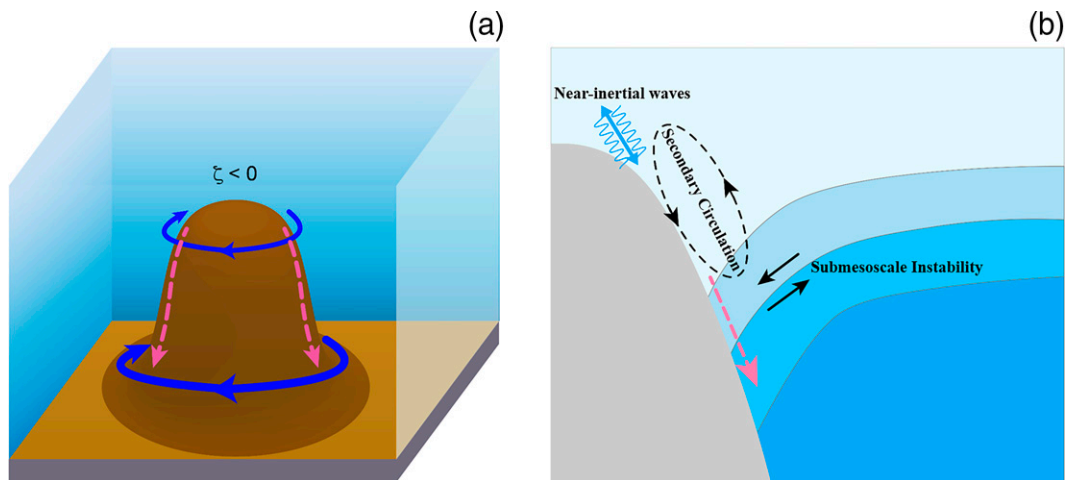
FIG. 7. (a) Schematic depicting the potential mechanisms for the damping of the anticyclonic circulation (blue arrows) trapped at a seamount. The circulation drives a downslope bottom Ekman transport (pink dashed arrows). (b) The downslope Ekman transport not only drives a secondary circulation that may cause submesoscale instabilities but also generates near-inertial waves with propagation direction parallel to the topographic slope, leading to the removal of kinetic energy from the anticyclonic circulation. Verification of the existence of submesoscale instabilities requires high-resolution observational networks.

$-\partial U/\partial y$ can be assumed to be negative approaching the sloping bottom based on a no-slip boundary condition (Ruan et al. 2021a). This assumption is partly verified by a high-resolution regional model of the northwestern Pacific Ocean, in which dominantly negative relative vorticity was diagnosed at the top and base of the CS [see Fig. 11 of Jiang et al. (2021)]. The observed BBL at MB is very close to the lateral boundary of the CS (only ~0.3 km for lowermost ACM). Then the second term of Ertel PV in Eq. (6), during the emergence of anticyclonic flows ($U \sim 0.05$ m s^{-1}), is estimated to be negative at 15 MAS ($\partial U/\partial y \sim 1.67 \times 10^{-4}$ s^{-1} and $f \sim 4 \times 10^{-5}$ s^{-1}). Therefore, centrifugal instability may arise in the BBL of MB.

With enhanced lateral buoyancy gradient and thus vertical geostrophic shear, the Ertel PV can also be dominated by the first term in Eq. (6) and turn negative. Then the geostrophic Richardson number derived from Eq. (6), $\mathrm{Ri}_g = N^2/S_g^2$ with $S_g = \partial U/\partial z$ denoting the vertical geostrophic shear, can be adopted to identify the condition for the occurrence of symmetric instabilities. When Ri_g drops below $1/(1 - \partial U/\partial y/f)$ and thus approaches unity, symmetric instabilities can develop (Wenegrat et al. 2018; Yankovsky et al. 2021). At MB, the secondary circulation driven by the Ekman forcing, as well as elevated mixing, eliminated bottom stratification and increased lateral buoyancy gradients. Consequently, low-frequency vertical shear S_g associated with U was intermittently elevated in the presence of anticyclonic flows, as shown in Fig. 3d. During these periods, S_g approached or even exceeded N (viz., $\mathrm{Ri}_g \lesssim 1$; Fig. 3d), hinting at the possibility of the excitement of symmetric instabilities. This process is analogous to the case of a downfront wind driving an Ekman transport that brings dense water over light water, leading to enhanced convection and development of symmetric instabilities (Thomas 2005; D'Asaro et al. 2011; Wenegrat and Thomas 2020).

c. A schematic diagram

Our observations captured the generation of resonant NIWs in the BBL of an abyssal seamount (Fig. 7). The bottom-intensified anticyclonic circulation trapped around the seamount produces a downslope Ekman transport (Fig. 7a). This downslope Ekman transport brings light water downward and gives rise to buoyancy forcing that acts against the Ekman transport, leading to the time-varying bottom stress. This stress generates NIWs propagating in parallel to the topographic slope (Fig. 7b). Although these bottom-generated NIWs, in theory, do not have a preferred propagation direction of upslope or downslope at generation, their further propagation in variable background stratification may be predominantly upward. On the other hand, the bottom Ekman forcing can induce a secondary circulation across the entire seamount slope, destroy bottom stratification, and then sharpen the lateral buoyancy gradient. As the near-bottom stratification is weakened and geostrophic shear is elevated, the near-bottom potential vorticity may be destroyed to stimulate submesoscale instabilities. Both resonant internal waves and submesoscale turbulence are expected to elevate dissipation and mixing near the BBL and promoting water exchange between the BBL and the interior over the seamount. It should be pointed out that the bottom Ekman forcing may not be the only mechanism driving the cross-isobath velocity V in Eq. (4). The cross-isobath flows driven by other processes in the BBL at sloping topography (e.g., wakes around the seamount; Jiang et al. 2021) may also alter the bottom stress, leading to generation of resonant internal waves.

6. Summary

Using moored observations carried out at the Caiwei Seamount in the northwest Pacific Ocean, we have examined

potential mechanisms for the damping of energetic near-bottom currents trapped by the seamount. The observed bottom currents flow dominantly in the direction of Kelvin wave propagation (i.e., anticyclonic in the Northern Hemisphere). Therefore, these currents can drive a downslope Ekman transport and give rise to an upslope buoyancy forcing that alters the bottom stress, leading to resonant generation of near-inertial waves in the BBL. Although these bottom-generated waves are partly dissipated near the seafloor, half of their energy subsequently radiates upward into the ocean interior, promoting mixing away from the seamount.

Bottom-intensified anticyclonic flows can also be found near other topographic features, such as the continental slopes (Merryfield and Scott 2007; Xie et al. 2018), bumps (Saunders and King 1995), and ridges (Lavelle et al. 2012; Liang and Thurnherr 2011). Therefore, the presented mechanism for the generation of NIWs may apply to most sloping topography in the global ocean. Although the cyclonic flows that generate the upslope Ekman transport is relatively rare near rough topography, the generation of NIWs by time-varying bottom stress may also occur in this case (Brink and Lentz 2010; Ruan et al. 2021b). It should be pointed out that internal waves are no longer near-inertial when the slope is steep [Eq. (4)]. However, the numerical simulations of Wenegrat and Thomas (2020) also showed the generation of superinertial internal waves with $\omega_c = 1.9f$ in the BBL (see their Fig. 5a; J. Wenegrat 2022, personal communication), suggesting the universality of internal-wave generation in the BBL over the sloping bottom.

Comparing the relative contribution of internal-wave generation with that of frictional drag dissipation to the energy loss of the bottom currents, we suggest an important role played by the former via the Ekman adjustment in dissipating geostrophic flows over a sloping seafloor. Using limited moored measurements, we speculate that the downslope Ekman transport may also induce submesoscale instabilities in the BBL, which may serve as another potential mechanism in damping the geostrophic circulation trapped by the seamount. However, high-resolution observations and numerical simulations are required in future work to verify the generation of near-bottom submesoscale instabilities in seamount systems and fully explore the mechanisms of energy cascades from bottom-trapped geostrophic circulations to small-scale turbulence.

Data availability statement. Bathymetry data are available in Guo et al. (2020). The filed data used in this study can be found at https://zenodo.org/record/6612676#.YprOF6hBx3g.

REFERENCES

Alford, M. H., J. A. MacKinnon, H. L. Simmons, and J. D. Nash, 2016: Near-inertial internal gravity waves in the ocean. *Annu. Rev. Fluid Mech.*, **8**, 95–123, https://doi.org/10.1146/annurev-marine-010814-015746.

Brearley, J. A., K. L. Sheen, A. C. Naveira Garabato, D. A. Smeed, and S. Waterman, 2013: Eddy-induced modulation of turbulent dissipation over rough topography in the Southern Ocean. *J. Phys. Oceanogr.*, **43**, 2288–2308, https://doi.org/10.1175/JPO-D-12-0222.1.

Brink, K. H., and S. J. Lentz, 2010: Buoyancy arrest and bottom Ekman transport. Part I: Steady flow. *J. Phys. Oceanogr.*, **40**, 621–635, https://doi.org/10.1175/2009JPO4266.1.

D'Asaro, E., C. Lee, L. Rainville, R. Harcourt, and L. Thomas, 2011: Enhanced turbulence and energy dissipation at ocean fronts. *Science*, **332**, 318–322, https://doi.org/10.1126/science.1201515.

Dewar, W. K., J. C. McWilliams, and M. J. Molemaker, 2015: Centrifugal instability and mixing in the California Undercurrent. *J. Phys. Oceanogr.*, **45**, 1224–1241, https://doi.org/10.1175/JPO-D-13-0269.1.

Freeland, H., 1994: Ocean circulation at and near Cobb Seamount. *Deep-Sea Res. I*, **41**, 1715–1732, https://doi.org/10.1016/0967-0637(94)90069-8.

Garrett, C., P. MacCready, and P. Rhines, 1993: Boundary mixing and arrested Ekman layers: Rotating stratified flow near a sloping boundary. *Annu. Rev. Fluid Mech.*, **25**, 291–323, https://doi.org/10.1146/annurev.fl.25.010193.001451.

Gula, J., M. J. Molemaker, and J. C. McWilliams, 2016: Topographic generation of submesoscale centrifugal instability and energy dissipation. *Nat. Commun.*, **7**, 12811, https://doi.org/10.1038/ncomms12811.

Guo, B., and Coauthors, 2020: Observed deep anticyclonic cap over Caiwei Guyot. *J. Geophys. Res. Oceans*, **125**, e2020JC016254, https://doi.org/10.1029/2020JC016254.

Haidvogel, D. B., A. Beckmann, D. C. Chapman, and R.-Q. Lin, 1993: Numerical simulation of flow around a tall isolated seamount. Part II: Resonant generation of trapped waves. *J. Phys. Oceanogr.*, **23**, 2373–2391, https://doi.org/10.1175/1520-0485(1993)023<2373:NSOFAA>2.0.CO;2.

Hu, Q., and Coauthors, 2020: Cascade of internal wave energy catalyzed by eddy-topography interactions in the deep South China Sea. *Geophys. Res. Lett.*, **47**, e2019GL086510, https://doi.org/10.1029/2019GL086510.

Jiang, X., C. Dong, Y. Ji, C. Wang, Y. Shu, L. Liu, and J. Ji, 2021: Influences of deep-water seamounts on the hydrodynamic environment in the northwestern Pacific Ocean. *J. Geophys. Res. Oceans*, **126**, e2021JC017396, https://doi.org/10.1029/2021JC017396.

Kunze, E., and T. B. Sanford, 1986: Near-inertial wave interactions with mean flow and bottom topography near Caryn Seamount. *J. Phys. Oceanogr.*, **16**, 109–120, https://doi.org/10.1175/1520-0485(1986)016<0109:NIWIWM>2.0.CO;2.

Lavelle, J. W., and C. Mohn, 2010: Motion, commotion, and biophysical connections at deep ocean seamounts. *Oceanography*, **23**, 90–103, https://doi.org/10.5670/oceanog.2010.64.

——, A. M. Thurnherr, L. S. Mullineaux, D. J. McGillicuddy Jr., and J. R. Ledwell, 2012: The prediction, verification, and significance of flank jets at mid-ocean ridges. *Oceanography*, **25**, 277–283, https://doi.org/10.5670/oceanog.2012.26.

Lentz, S. J., and J. H. Trowbridge, 1991: The bottom boundary layer over the continental shelf. *J. Phys. Oceanogr.*, **21**,

1186–1201, https://doi.org/10.1175/1520-0485(1991)021<1186:TBBLOT>2.0.CO;2.

Liang, X., and A. M. Thurnherr, 2011: Subinertial variability in the deep ocean near the east Pacific rise between 98° and 108°N. *Geophys. Res. Lett.*, **38**, L06606, https://doi.org/10.1029/2011GL046675.

——, and ——, 2012: Eddy-modulated internal waves and mixing on a midocean ridge. *J. Phys. Oceanogr.*, **42**, 1242–1248, https://doi.org/10.1175/JPO-D-11-0126.1.

MacCready, P., and P. B. Rhines, 1991: Buoyant inhibition of Ekman transport on a slope and its effect on stratified spin-up. *J. Fluid Mech.*, **223**, 631–661, https://doi.org/10.1017/S0022112091001581.

——, and ——, 1993: Slippery bottom boundary layers on a slope. *J. Phys. Oceanogr.*, **23**, 5–22, https://doi.org/10.1175/1520-0485(1993)023<0005:SBBLOA>2.0.CO;2.

Merryfield, W. J., and R. B. Scott, 2007: Bathymetric influence on mean currents in two high-resolution near-global models. *Ocean Modell.*, **16**, 76–94, https://doi.org/10.1016/j.ocemod.2006.07.005.

Moum, J. N., A. Perlin, J. K. Klymak, M. D. Levine, T. Boyd, and P. M. Kosro, 2004: Convectively driven mixing in the bottom boundary layer. *J. Phys. Oceanogr.*, **34**, 2189–2202, https://doi.org/10.1175/1520-0485(2004)034<2189:CDMITB>2.0.CO;2.

Naveira Garabato, A. C., and Coauthors, 2019: Rapid mixing and exchange of deep-ocean waters in an abyssal boundary current. *Proc. Natl. Acad. Sci. USA*, **116**, 13233–13238, https://doi.org/10.1073/pnas.1904087116.

Nikurashin, M., and R. Ferrari, 2010a: Radiation and dissipation of internal waves generated by geostrophic motions impinging on small-scale topography: Application to the Southern Ocean. *J. Phys. Oceanogr.*, **40**, 2025–2042, https://doi.org/10.1175/2010JPO4315.1.

——, and ——, 2010b: Radiation and dissipation of internal waves generated by geostrophic motions impinging on small-scale topography: Theory. *J. Phys. Oceanogr.*, **40**, 1055–1074, https://doi.org/10.1175/2009JPO4199.1.

Pinkel, R., 1984: Doppler sonar observations of internal waves: The wavenumber-frequency spectrum. *J. Phys. Oceanogr.*, **14**, 1249–1275, https://doi.org/10.1175/1520-0485(1984)014<1249:DSOOIW>2.0.CO;2.

Polzin, K. L., B. Wang, Z. Wang, F. Thwaites, and A. J. Williams, 2021: Moored flux and dissipation estimates from the northern deepwater Gulf of Mexico. *Fluids*, **6**, 237, https://doi.org/10.3390/fluids6070237.

Ruan, X., A. F. Thompson, and J. R. Taylor, 2019: The evolution and arrest of a turbulent stratified oceanic bottom boundary layer over a slope: Downslope regime. *J. Phys. Oceanogr.*, **49**, 469–487, https://doi.org/10.1175/JPO-D-18-0079.1.

——, J. O. Wenegrat, and J. Gula, 2021a: Slippery bottom boundary layers: The loss of energy from the general circulation by bottom drag. *Geophys. Res. Lett.*, **48**, e2021GL094434, https://doi.org/10.1029/2021GL094434.

——, A. F. Thompson, and J. R. Taylor, 2021b: The evolution and arrest of a turbulent stratified oceanic bottom boundary layer over a slope: Upslope regime and PV dynamics. *J. Phys. Oceanogr.*, **51**, 1077–1089, https://doi.org/10.1175/JPO-D-20-0168.1.

Saunders, P. M., and B. A. King, 1995: Bottom currents derived from a shipborne ADCP on WOCE cruise A11 in the South Atlantic. *J. Phys. Oceanogr.*, **25**, 329–347, https://doi.org/10.1175/1520-0485(1995)025<0329:BCDFAS>2.0.CO;2.

Sen, A., R. B. Scott, and B. K. Arbic, 2008: Global energy dissipation rate of deep-ocean low-frequency flows by quadratic bottom boundary layer drag: Computations from current-meter data. *Geophys. Res. Lett.*, **35**, L09606, https://doi.org/10.1029/2008GL033407.

Sheen, K. L., and Coauthors, 2013: Rates and mechanisms of turbulent dissipation and mixing in the Southern Ocean: Results from the diapycnal and isopycnal mixing experiment in the Southern Ocean (DIMES). *J. Geophys. Res. Oceans*, **118**, 2774–2792, https://doi.org/10.1002/jgrc.20217.

Stahr, F. R., and T. B. Sanford, 1999: Transport and bottom boundary layer observations of the North Atlantic deep western boundary current at the Blake Outer Ridge. *Deep-Sea Res. II*, **46**, 205–243, https://doi.org/10.1016/S0967-0645(98)00101-5.

Thomas, L. N., 2005: Destruction of potential vorticity by winds. *J. Phys. Oceanogr.*, **35**, 2457–2466, https://doi.org/10.1175/JPO2830.1.

——, J. R. Taylor, R. Ferrari, and T. M. Joyce, 2013: Symmetric instability in the Gulf Stream. *Deep-Sea Res. II*, **91**, 96–110, https://doi.org/10.1016/j.dsr2.2013.02.025.

Trowbridge, J. H., and S. J. Lentz, 1991: Asymmetric behavior of an oceanic boundary layer above a sloping bottom. *J. Phys. Oceanogr.*, **21**, 1171–1185, https://doi.org/10.1175/1520-0485(1991)021<1171:ABOAOB>2.0.CO;2.

——, and ——, 2018: The bottom boundary layer. *Annu. Rev. Fluid Mech.*, **10**, 397–420, https://doi.org/10.1146/annurev-marine-121916-063351.

Umlauf, L., W. D. Smyth, and J. N. Moum, 2015: Energetics of bottom Ekman layers during buoyancy arrest. *J. Phys. Oceanogr.*, **45**, 3099–3117, https://doi.org/10.1175/JPO-D-15-0041.1.

van Aken, H. M., L. R. M. Maas, and H. van Haren, 2005: Observations of inertial wave events near the continental slope off Goban Spur. *J. Phys. Oceanogr.*, **35**, 1329–1340, https://doi.org/10.1175/JPO2769.1.

van Haren, H., 2004: Bandwidth similarity at inertial and tidal frequencies in kinetic energy spectra from the Bay of Biscay. *Deep-Sea Res. I*, **51**, 637–652, https://doi.org/10.1016/j.dsr.2004.01.006.

Weatherly, G. L., and P. J. Martin, 1978: On the structure and dynamics of the oceanic bottom boundary layer. *J. Phys. Oceanogr.*, **8**, 557–570, https://doi.org/10.1175/1520-0485(1978)008<0557:OTSADO>2.0.CO;2.

Wenegrat, J. O., and L. N. Thomas, 2020: Centrifugal and symmetric instability during Ekman adjustment of the bottom boundary layer. *J. Phys. Oceanogr.*, **50**, 1793–1812, https://doi.org/10.1175/JPO-D-20-0027.1.

——, J. Callies, and L. N. Thomas, 2018: Submesoscale baroclinic instability in the bottom boundary layer. *J. Phys. Oceanogr.*, **48**, 2571–2592, https://doi.org/10.1175/JPO-D-17-0264.1.

Wright, C. J., R. B. Scott, D. Furnival, P. Ailliot, and F. Vermet, 2013: Global observations of ocean-bottom subinertial current dissipation. *J. Phys. Oceanogr.*, **43**, 402–417, https://doi.org/10.1175/JPO-D-12-082.1.

Wunsch, C., and R. Ferrari, 2004: Vertical mixing, energy, and the general circulation of the oceans. *Annu. Rev. Fluid Mech.*, **36**, 281–314, https://doi.org/10.1146/annurev.fluid.36.050802.122121.

Xie, X., and M. Li, 2019: Generation of internal lee waves by lateral circulation in a coastal plain estuary. *J. Phys. Oceanogr.*, **49**, 1687–1697, https://doi.org/10.1175/JPO-D-18-0142.1.

——, ——, M. Scully, and W. C. Boicourt, 2017: Generation of internal solitary waves by lateral circulation in a stratified estuary. *J. Phys. Oceanogr.*, **47**, 1789–1797, https://doi.org/10.1175/JPO-D-16-0240.1.

——, Q. Liu, Z. Zhao, X. Shang, S. Cai, D. Wang, and D. Chen, 2018: Deep sea currents driven by breaking internal tides on the continental slope. *Geophys. Res. Lett.*, **45**, 6160–6166, https://doi.org/10.1029/2018GL078372.

——, and Coauthors, 2022: Enhanced near-bottom circulation and mixing driven by the surface eddies over abyssal seamounts. *Prog. Oceanogr.*, **208**, 102896, https://doi.org/10.1016/j.pocean.2022.102896.

——, X. Liu, Z. Chen, Y. Wang, D. Chen, W. Li, and D. Zhang, 2023: Pure inertial waves radiating from low-frequency flows over large-scale topography. *Geophys. Res. Lett.*, https://doi.org/10.1029/2022GL099889, in press.

Yankovsky, E., S. Legg, and R. Hallberg, 2021: Parameterization of submesoscale symmetric instability in dense flows along topography. *J. Adv. Model. Earth Syst.*, **13**, e220MS002264, https://doi.org/10.1029/2020MS002264.